



# Enhanced photocatalytic activity and stability of Z-scheme Ag<sub>2</sub>CrO<sub>4</sub>-GO composite photocatalysts for organic pollutant degradation

Difa Xu<sup>a,b</sup>, Bei Cheng<sup>a</sup>, Shaowen Cao<sup>a,\*</sup>, Jiaguo Yu<sup>a,\*</sup>

<sup>a</sup> State Key Laboratory of Advanced Technology for Materials Synthesis and Processing, Wuhan University of Technology, Wuhan 430070, PR China

<sup>b</sup> Hunan Province Key Laboratory of Applied Environmental Photocatalysis, Changsha University, Changsha 410022, PR China

## ARTICLE INFO

### Article history:

Received 20 July 2014

Received in revised form

14 September 2014

Accepted 19 September 2014

Available online 28 September 2014

### Keywords:

Graphene oxide

Ag<sub>2</sub>CrO<sub>4</sub>

Photocatalysis

Z-scheme

Heterojunction

## ABSTRACT

Silver chromate-graphene oxide (Ag<sub>2</sub>CrO<sub>4</sub>-GO) composites are prepared by a facile precipitation method. The resulting Ag<sub>2</sub>CrO<sub>4</sub>-GO composites exhibit excellent photocatalytic activity and stability towards the degradation of the dyes and phenol in aqueous solution under visible-light irradiation. The optimal composite with 1.0 wt% GO content shows the highest photocatalytic activity for methylene blue (MB) degradation, which is 3.5 times that of pure Ag<sub>2</sub>CrO<sub>4</sub> particles. The enhanced photocatalytic activity is mainly attributed to the formation of Ag<sub>2</sub>CrO<sub>4</sub>-GO Z-scheme heterojunction that can not only facilitate the separation and transfer of the photogenerated charge carriers, but also preserve a strong oxidation and reduction ability. The high photocatalytic stability is due to the successful inhibition of the photocorrosion of Ag<sub>2</sub>CrO<sub>4</sub> by transferring the photogenerated electrons of Ag<sub>2</sub>CrO<sub>4</sub> to GO. The present work provides a new understanding into design and fabrication of the GO/silver compound composite photocatalysts.

© 2014 Elsevier B.V. All rights reserved.

## 1. Introduction

With the increasing deterioration of global environment, it is urgent to develop feasible techniques to eliminate the environmental contamination caused by organic pollutants. Although conventional physical, chemical and biological methods are established for wastewater treatment, it is still difficult for them to remove the organic pollutants with high toxicity but very low concentration from water [1]. Semiconductor photocatalysis, a green technique that can decompose the organic pollutants into non-hazardous compounds using semiconductor photocatalysts under light irradiation, provides a new option to address the above challenges. It is known that TiO<sub>2</sub> has excellent photocatalytic activity and stability, but is only active under ultraviolet light irradiation because of its wide band gap. Therefore, many attentions are focused on the development of novel visible-light active photocatalysts. In recent years, silver compounds have attracted much interest due to their excellent light sensitivity and high photocatalytic activity [2,3]. A variety of silver compounds, such as silver halides (AgX, X=Cl, Br, I), silver-containing oxides (Ag<sub>3</sub>PO<sub>4</sub>,

Ag<sub>2</sub>CO<sub>3</sub>, AgGaO<sub>2</sub>, Ag<sub>2</sub>CrO<sub>4</sub>), Ag<sub>2</sub>S and Ag<sub>2</sub>Se, have shown the ability to decompose the organic pollutants under visible-light irradiation [3]. Among them, Ag<sub>2</sub>CrO<sub>4</sub> is recognized as a promising candidate due to its unique electronic structure and crystal structure [4–7]. Particularly, the valence band (VB) position of Ag<sub>2</sub>CrO<sub>4</sub> is raised by the hybridization of Ag 4d and O 2p orbital, and the conduction band (CB) position is lowered by Cr element, resulting in a narrow band gap of ~1.80 eV [7]. Moreover, the crystal structure of Ag<sub>2</sub>CrO<sub>4</sub> is favourable for the effective migration of charge carriers due to its long Ag–O bond length (~2.438 Å) and big O–Ag–O bond angle (~180°) of AgO<sub>6</sub> octahedron [4]. Very recently, we have demonstrated the good visible-light photocatalytic activity of Ag<sub>2</sub>CrO<sub>4</sub> for the decomposition of organic dyes in aqueous solution [7]. Nevertheless, similar to many other silver compounds, the photocorrosion of Ag<sub>2</sub>CrO<sub>4</sub> occurs during the photocatalytic reactions, seriously destroying the structure of the photocatalyst. Hence, it is highly desirable to find effective ways to inhibit the photocorrosion of Ag<sub>2</sub>CrO<sub>4</sub> for better stability and activity.

Generally, to improve the photocatalytic activity and stability of silver compounds, it is necessary to rapidly transfer the photogenerated electrons from the surface of silver compounds to an acceptor material before Ag<sup>+</sup> is reduced to metallic Ag<sup>0</sup> [8]. As a novel cousin of graphene, graphene oxide (GO) has received considerable attentions owing to its extremely large specific surface area, high thermal and chemical stability, and excellent mobility

\* Corresponding authors. Tel.: +86 27 87871029; fax: +86 27 87879468.

E-mail addresses: [swcao@whut.edu.cn](mailto:swcao@whut.edu.cn) (S. Cao), [jiaguoyu@yahoo.com](mailto:jiaguoyu@yahoo.com), [yujiaguoyu93@163.com](mailto:yujiaguoyu93@163.com) (J. Yu).

of charge carriers, which enable GO to be one of the most ideal supports for the separation and transfer of the photogenerated charge carriers [9,10]. Thus, a variety of GO-based photocatalysts, such as TiO<sub>2</sub>-GO [11–14], ZnO-GO [15], CdS-GO [16,17], BiOBr-GO [18,19], MnO<sub>2</sub>-GO [20,21], AgX (X=Cl,Br)-GO [22–25], Ag<sub>3</sub>PO<sub>4</sub>-GO [26–28] and Ag<sub>2</sub>CO<sub>3</sub>-GO [29,30], are developed for photocatalytic hydrogen production and organic pollutant degradation. In addition, it is demonstrated that GO can also serve as a photocatalyst for hydrogen evolution from water reduction due to its negative conduction band position [31,32]. Thus, it is possible to construct a Z-scheme Ag<sub>2</sub>CrO<sub>4</sub>-GO composite photocatalyst with enhanced photocatalytic activity and stability.

Herein, we for the first time report the preparation of Z-scheme Ag<sub>2</sub>CrO<sub>4</sub>-GO composite photocatalyst via a facile precipitation method without any surfactant. Comparing with the pure Ag<sub>2</sub>CrO<sub>4</sub> particles, the obtained Ag<sub>2</sub>CrO<sub>4</sub>-GO composites showed distinctly enhanced photocatalytic activity on the degradation of dyes and phenol under visible-light irradiation. Noticeably, the photocorrosion of Ag<sub>2</sub>CrO<sub>4</sub> was efficiently inhibited due to the introduction of GO as electron transfer medium and acceptor. It is worth noting that the photocatalytic reaction in the presence of Ag<sub>2</sub>CrO<sub>4</sub>-GO composites followed a Z-scheme mechanism. A Z-scheme photocatalyst is a type of heterostructured photocatalyst possessing high charge-separation efficiency and strong redox ability [33,34]. Our investigation will enrich the studies of GO-based photocatalysts and inspire the exploration of silver compound-based photocatalysts with high photocatalytic activity and stability.

## 2. Experimental

### 2.1. Materials

All chemicals were analytical grade and purchased from Shanghai Chemical Reagent Factory of China without further purification. Deionized (DI) water was used in the whole experiment.

### 2.2. Preparation

GO was synthesized from natural graphite powder (>99.8%, Alfa Aesar). Briefly, 3 g of graphite was introduced into a mixture of concentrated H<sub>2</sub>SO<sub>4</sub> (15 mL), K<sub>2</sub>S<sub>2</sub>O<sub>8</sub> (2.5 g), and P<sub>2</sub>O<sub>5</sub> (2.5 g). The solution was heated to 80 °C and kept stirring for 8 h. After the solution was cooled to room temperature and diluted by 500 mL of DI water, the product was filtered using 0.2 μm Nylon Millipore filter and dried under ambient condition. This pre-oxidized graphite was oxidized according to Hummers and Offeman methods to produce GO [35], which was dried and stored as the form of powders.

The Ag<sub>2</sub>CrO<sub>4</sub>-GO composites were synthesized by a self-assembly precipitation method under the dark conditions. The formation procedure for the Ag<sub>2</sub>CrO<sub>4</sub> enwrapped with GO is proposed in Scheme 1. Typically, 80 mg of GO was dispersed into 80 mL of DI water and then ultrasonically treated for 2 h to obtain a GO aqueous suspension with a concentration of 1.0 mg mL<sup>-1</sup>. A known amount of GO aqueous suspension was added to 100 mL of AgNO<sub>3</sub> solution (0.06 mol L<sup>-1</sup>) and stirred for 12 h to ensure the positively charged Ag<sup>+</sup> being adsorbed on the surface of negatively charged GO via electrostatic interaction. Then 100 mL of K<sub>2</sub>CrO<sub>4</sub> solution (0.03 mol L<sup>-1</sup>) was dripped into the mixture and kept stirring for 1 h. After aging at room temperature for 4 h, the obtained brick-red precipitate was collected by centrifugation, washed with DI water for six times, and then dried in oven at 80 °C for 6 h. To investigate the optimal GO loading amount, a series of samples with theoretical weight ratios of GO to Ag<sub>2</sub>CrO<sub>4</sub> (0, 0.5, 0.75, 1, 2 and 3 wt%) were obtained, and the corresponding final products were denoted as Gx (x=0, 0.5, 0.75, 1, 2 and 3). For the purpose of comparison, N-doped

TiO<sub>2</sub> (TiO<sub>1.98</sub>N<sub>0.02</sub>: N-TiO<sub>2</sub>) photocatalyst was prepared according to the previous report method and used as the reference catalyst [36].

### 2.3. Characterization

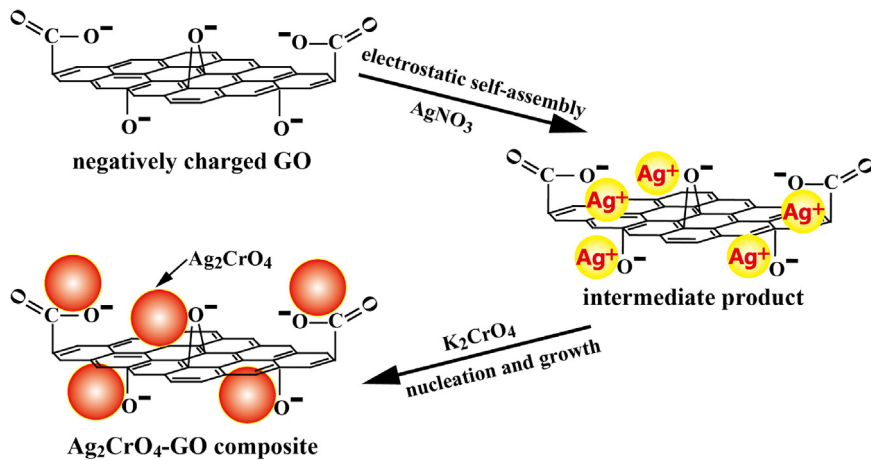
The X-ray diffraction (XRD) patterns were recorded on an X-ray diffractometer (type HZG41BPC) with Cu K $\alpha$  irradiation source ( $\lambda = 0.15418$  nm) at a scan rate ( $2\theta$ ) of  $0.05^\circ$  s<sup>-1</sup>. The accelerating voltage and the applied current were 40 kV and 80 mA, respectively. Raman analysis was carried out on a micro-Raman spectrometer (RenishawInVia) in the back-scattering geometry of 514.5 nm Ar<sup>+</sup> laser as an excitation source. The morphology observation was conducted on an S4800 field emission scanning electron microscope (FESEM, Hitachi, Japan) at an accelerating voltage of 5 kV. Transmission electron microscopy (TEM) images were obtained on a JEM-2100F electron microscopy (JEOL, Japan), using a 200 kV accelerating voltage. The nitrogen adsorption and desorption isotherms of the samples were measured by an ASAP 2020 nitrogen adsorption apparatus (Micromeritics Instruments, USA) after the samples were subjected to a degassing treatment at 180 °C for 12 h. The Brunauer–Emmett–Teller (BET) surface area ( $S_{BET}$ ) of the samples was determined by a multi-point BET method using the adsorption data in the relative pressure ( $P/P_0$ ) range of 0.05–0.3. The pore size distribution of the samples was determined by assuming cylindrical pore model using Barret–Joyner–Halender (BJH) method. The pore volume and average pore size were determined by the nitrogen adsorption volume at the relative pressure ( $P/P_0$ ) of 0.994. The UV-vis diffuse reflectance spectra (DRS) of the samples were obtained with a UV-vis spectrophotometer (UV2550, Shimadzu, Japan). BaSO<sub>4</sub> was used as a reflectance standard. The Zeta potential was measured by electrophoretic light scattering with a zetasizer (nano ZS90, Malvern, UK). X-ray photoelectron spectroscopy (XPS) was investigated with ultrahigh vacuum VG EXCALAB 210 electron spectrometer using Mg K $\alpha$  (1253.6 eV) as radiation source.

### 2.4. Photoelectrochemistry measurement

Electrochemical impedance spectroscopy (EIS) measurements were obtained using a CHI660C electrochemical workstation (Chenhua Instruments, Shanghai, China). The measurement was conducted in a conventional three-electrode cell system. Namely, the samples were deposited on fluorine-tin oxide (FTO) glass by using doctor-blade technique to serve as the working electrodes (1.5 cm<sup>2</sup> active area). A Pt electrode, an Ag/AgCl electrode and 0.5 M potassium nitrate were employed as the counter electrode, the reference electrode and the electrolyte, respectively. The same electrochemical system was employed to determine the flat-band potential of the working electrodes (pure Ag<sub>2</sub>CrO<sub>4</sub> or Ag<sub>2</sub>CrO<sub>4</sub>-GO composites) by the Mott–Schottky (MS) method. The measurements were performed in darkness by scanning the electrode potential from -0.5 to 1.0 V at a scan rate of 25 mV/s, and the impedance–potential characteristics were recorded at a frequency of 1 kHz.

### 2.5. Photocatalytic activity measurement

Photocatalytic activity of the as-prepared samples was evaluated by the photocatalytic degradation of the dye and phenol aqueous solution under visible-light irradiation. The photocatalytic reaction was carried out in an open reactor with a diameter of 90 mm and the reaction temperature was about 25 °C. 20 mg of the photocatalyst was ultrasonically dispersed in 100 mL of MB aqueous solution ( $1 \times 10^{-5}$  mol L<sup>-1</sup>) for 10 min and then stirred in the dark for 1 h to achieve the adsorption–desorption equilibrium. A 300 W simulated solar Xe arc lamp (Changzhou Siyu Technic Co.,



**Scheme 1.** Schematic illustration of the Ag<sub>2</sub>CrO<sub>4</sub>-GO composites synthesized by a facile self-assembly precipitation method without any surfactant.

China) with a 400 nm cut-off filter was employed as the visible-light source. The vertical distance between the light source and the surface of the solution was ~25 cm. About 4 mL of suspension was taken out at regular time intervals under irradiation and separated through centrifugation (5000 rpm, 15 min). To investigate the universality of the obtained samples on the organic pollutant degradation, the same operations were carried out except that the MB aqueous solution was replaced by 100 mL of Rhodamine B (RhB,  $1 \times 10^{-5}$  mol L<sup>-1</sup>), methyl orange (MO,  $1 \times 10^{-5}$  mol L<sup>-1</sup>) and phenol ( $5 \text{ mg L}^{-1}$ ) aqueous solution, respectively. The concentration of MB, RhB and MO was determined by a UV-vis spectrophotometer (UV2550, Shimadzu, Japan) at the wavelength of 663, 553 and 460 nm, respectively. The concentration of phenol was monitored by colorimetric method using 4-aminoantipyrine as the colour-developing agent at the wavelength of 510 nm [37]. To investigate the photocatalytic stability of the samples, the photocatalytic activity measurement was repeated by the same procedure as mentioned above but using 200 mg of photocatalyst and 200 mL of MB aqueous solution ( $2 \times 10^{-5}$  mol L<sup>-1</sup>). After each run of photocatalytic reaction, the concentrated MB solution was injected and the separated photocatalysts were washed and used again in order to keep the initial concentration of MB and photocatalysts un-polluted [38]. As for the dye and phenol aqueous solution with low concentration, the photocatalytic degradation was a pseudo-first-order reaction and the kinetics was expressed as  $\ln(C_0/C_t) = kt$ , where  $k$  is the apparent rate constant,  $C_0$  is the initial concentration of the pollutant after the adsorption-desorption equilibrium and  $C_t$  is the residual concentration of the pollutant collected at regular time intervals under visible-light irradiation. The photocatalytic activity of TiO<sub>1.98</sub>N<sub>0.02</sub> was also measured as a reference. To further investigate the photocatalytic mechanism, trapping experiments were performed to determine the dominant reactive species involved in the photodegradation of MB dye. The experimental procedure was similar to the photocatalytic activity measurement, except that 100 mL of MB aqueous solution was replaced by 100 mL of mixture of the dye and scavenger.

### 3. Results and discussion

#### 3.1. Phase structure and morphology

Typical XRD patterns of the pure Ag<sub>2</sub>CrO<sub>4</sub> sample and Ag<sub>2</sub>CrO<sub>4</sub>-GO composites with different weight ratios of GO are shown in Fig. 1. It can be seen that all samples possess similar XRD patterns and all diffraction peaks can be indexed to the orthorhombic phase of Ag<sub>2</sub>CrO<sub>4</sub> (JCPDS No. 26-0952). It is noted that the peaks

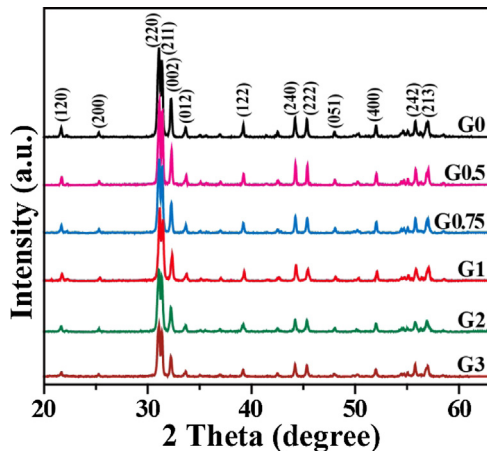


**Fig. 1.** XRD patterns of G0, G0.5, G0.75, G1, G2 and G3.

become broader with increasing the GO content, which is similar to the previous observation [17], indicating the successful immobilization and limited growth of Ag<sub>2</sub>CrO<sub>4</sub> particles on the surface of GO nanosheets [17,39]. No characteristic diffraction peak for carbon species is observed in the patterns because of the low amount and relatively low diffraction intensity of GO in the composites [16].

Raman spectra were used to verify the existence of carbon in the composites. As shown in Fig. 2, the Raman spectrum of

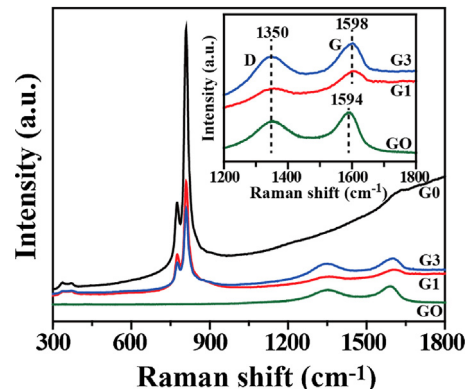


**Fig. 2.** Raman spectra of G0, G1, G3 and GO. The inset is the magnified Raman spectra of G1, G3 and GO in the region of 1200–1800 cm<sup>-1</sup>.

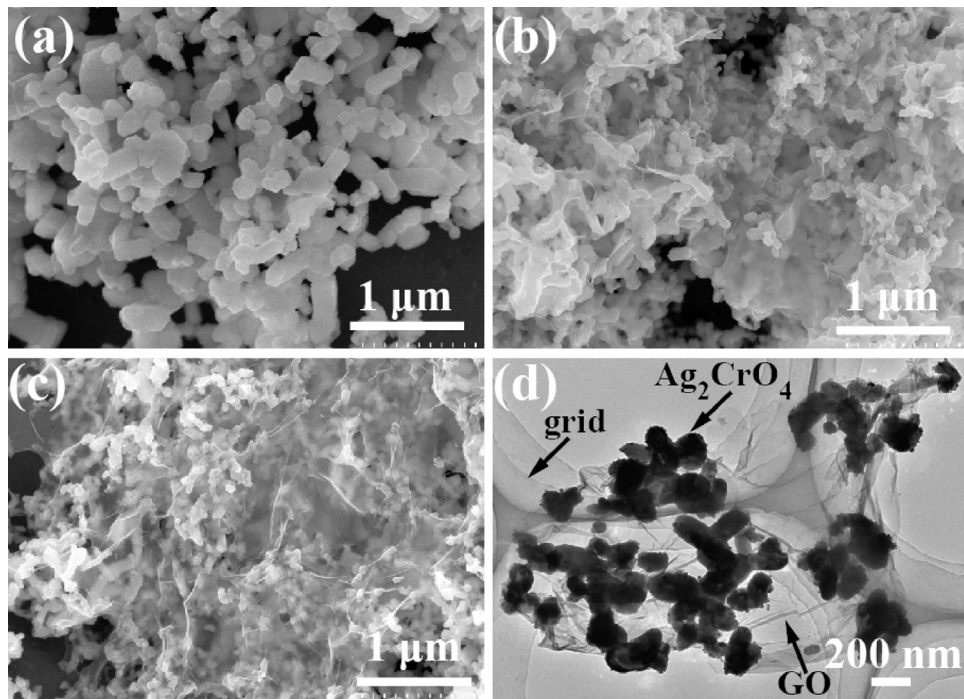


**Fig. 3.** Typical SEM images of (a) G0, (b) G1 and (c) G3, and (d) TEM image of G1.

GO shows the presence of D band at  $1350\text{ cm}^{-1}$  and G band at  $1594\text{ cm}^{-1}$ , corresponding to the breathing mode of *k*-point phonons of  $\text{A}_{1g}$  symmetry and the first-order scattering of  $E_{2g}$  vibration mode of  $\text{sp}^2$ -bonded carbon atoms [15,40], respectively. The Raman spectrum of  $\text{Ag}_2\text{CrO}_4$  is similar to that reported previously [41]. Specifically, the most intense peaks in the high-frequency region between  $750$  and  $900\text{ cm}^{-1}$  are the stretching modes of  $\text{CrO}_4$  group, and the considerable weaker peaks in the medium-frequency region between  $300$  and  $400\text{ cm}^{-1}$  can be ascribed to the bending modes of the  $\text{CrO}_4$  group [41,42]. The Raman spectra of G1 and G3 show both the characteristic Raman peaks of GO and  $\text{Ag}_2\text{CrO}_4$ , implying that the  $\text{Ag}_2\text{CrO}_4$  particles are successfully anchored onto the GO support. Moreover, the intensity of D/G ratio among G1, G3 and GO shown in the insert of Fig. 2 has no obvious change, indicating that GO participates in the formation of  $\text{Ag}_2\text{CrO}_4$ -GO composites via a non-destructive coalescent approach [17,43,44].

SEM and TEM are used to investigate the morphology of the obtained samples, as shown in Fig. 3. The average particle size of pure  $\text{Ag}_2\text{CrO}_4$  is ca.  $400\text{ nm}$  (Fig. 3a). While the  $\text{Ag}_2\text{CrO}_4$  particles in the  $\text{Ag}_2\text{CrO}_4$ -GO composites are much smaller and closely enwrapped by the gauze-like GO sheets (Fig. 3b and c). Such morphology evolution is further demonstrated by the TEM image of G1, which shows the  $\text{Ag}_2\text{CrO}_4$  particles with an average size of ca.  $200\text{ nm}$  anchoring to the surface of the transparent and wrinkled GO sheets (Fig. 3d).

It is found that the particle size of  $\text{Ag}_2\text{CrO}_4$  obviously decreased after the introduction of GO. This is consistent with the above XRD results because GO can serve as capping agent for inhibiting  $\text{Ag}_2\text{CrO}_4$  growth [25,26,45–47]. As is well known, GO possesses abundant negatively charged groups, which allow positively charged  $\text{Ag}^+$  to be adsorbed on the surface of GO via electrostatic interaction [22,26], to generate nucleation centres for  $\text{Ag}_2\text{CrO}_4$  growth. After the addition of  $\text{CrO}_4^{2-}$ , the formed  $\text{Ag}_2\text{CrO}_4$  could be anchored onto the surface of GO, suppressing the aggregation of the particles. The smaller particle size of  $\text{Ag}_2\text{CrO}_4$  in the presence of GO is beneficial for the improvement of the photocatalytic activity due to the enhanced interface contact area between  $\text{Ag}_2\text{CrO}_4$

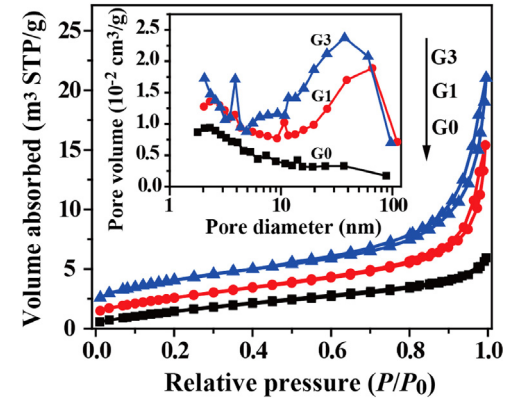


**Fig. 4.**  $\text{N}_2$  adsorption–desorption isotherms and corresponding pore-size distribution curves (inset) of G0, G1 and G3.

and GO. In addition, we have measured the zeta potential of the samples, indicating an absolute value of zeta potential increases with increasing the GO content (Table 1).

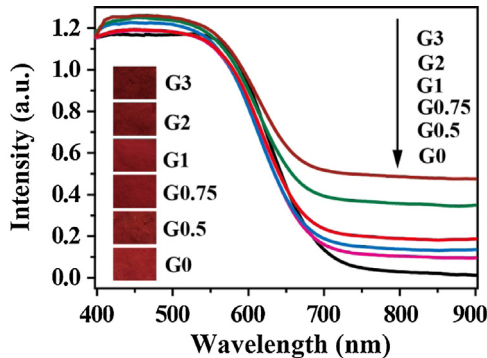
### 3.2. BET surface area and pore size distributions

To understand the effect of GO on the pore structure and specific surface area of  $\text{Ag}_2\text{CrO}_4$ ,  $\text{N}_2$  adsorption–desorption isotherms of G0, G1 and G3 and their corresponding pore-size distributions are investigated, as displayed in Fig. 4. According to the Brunauer–Deming–Deming–Teller classification,  $\text{N}_2$  adsorption–desorption isotherms of all samples are of type IV, indicating the presence of mesopores [48]. Moreover, the nonlimiting adsorption at high  $P/P_0$  is a characteristic of the type H3 loop, suggesting the formation of slitlike pores due to the aggregation of the plate-like particles [48]. Pore-size distributions were calculated using the BJH method from the adsorption branch of the isotherms. As shown in the inset of Fig. 4, G1 and G3 exhibit bimodal distributions with the pore size centred at  $10, 80\text{ nm}$  and  $4, 50\text{ nm}$ , respectively, suggesting the hard aggregates in the composites [49].

**Table 1**

Physicochemical property of as-prepared samples.

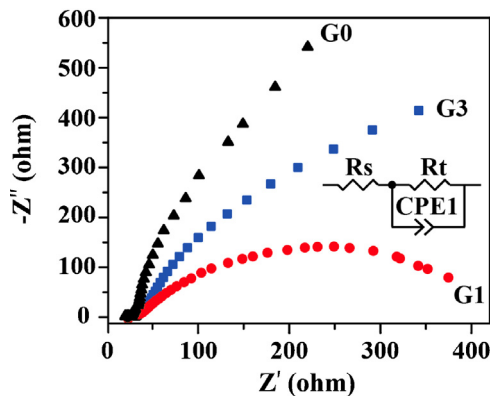
Samples	$S_{\text{BET}}$ ( $\text{m}^2/\text{g}$ )	Pore volume ( $\text{cm}^3/\text{g}$ )	Pore size (nm)	Zeta potential (mV)
G0	4	0.007	6.74	-13.5 ± 0.2
G0.5	6	0.008	5.23	-14.6 ± 0.3
G0.75	8	0.013	6.27	-16.2 ± 0.4
G1	10	0.015	6.54	-17.6 ± 0.2
G2	11	0.016	6.17	-21.6 ± 0.4
G3	15	0.023	6.32	-25.2 ± 0.9
GO	91	0.063	2.78	-30.1 ± 0.6

**Fig. 5.** UV-visible diffuse reflectance spectra and the corresponding colours (inset) of G0, G0.5, G0.75, G1, G2 and G3.

The pore size centred at 4 and 10 nm further confirms the existence of mesopores, which are from small intra-aggregation pores of  $\text{Ag}_2\text{CrO}_4$  particles. Meanwhile, the pore size centred at 50 and 80 nm represents the presence of macropores, which are ascribed to the large inter-aggregation of  $\text{Ag}_2\text{CrO}_4$ -GO composites. However, G0 exhibits a very broad pore-size distribution mainly resulting from the aggregations among  $\text{Ag}_2\text{CrO}_4$  particles [7]. Meanwhile, the BET specific surface area of the composite samples increases from 4 to 15  $\text{m}^2/\text{g}$  with increasing the GO content from 0 to 3 wt% (see Table 1). Combined with the SEM and TEM results, it can be seen that GO is an ideal support for the growth of  $\text{Ag}_2\text{CrO}_4$  particles with small sizes, leading to the formation of  $\text{Ag}_2\text{CrO}_4$ -GO composites with large surface contact area and enhanced pore volume.

### 3.3. UV-vis spectroscopy

A comparison of UV-vis diffuse reflectance spectra and the corresponding colour of the samples are displayed in Fig. 5 and its inset, respectively. Pure  $\text{Ag}_2\text{CrO}_4$  shows a sharp absorption edge at ~700 nm, corresponding to the band gap of ~1.8 eV. It should be noted that the absorption edge has no significant shift for all the other samples, indicating that GO in the composites is free carbon instead of the incorporated carbon, which results in a broad background absorption in the visible-light region rather than an absorption edge change [28,50]. Thus, the photo-absorption intensities of the composites are strengthened gradually in the range of 700–900 nm. This is in good agreement with the colour change of the samples, which turns to darker and darker with increasing the GO content (inset of Fig. 5). The strengthened photo-absorption of the composites could be not only attributed to the presence of GO that reduces the reflection of light [51,52], but also in relation to the possible electronic transition of  $\pi \rightarrow \pi^*$  of GO and  $n \rightarrow \pi^*$  between the n-orbit of the oxygen species of semiconductors and GO [17,53,54]. Therefore, it can be inferred that the introduction of GO would facilitate the photo-adsorption of  $\text{Ag}_2\text{CrO}_4$  particles and the separation of photogenerated charge carriers, resulting in enhanced photocatalytic activity of the composites.

**Fig. 6.** Typical electrochemical impedance spectra of G0, G1 and G3 under visible-light irradiation ( $\lambda \geq 400 \text{ nm}$ ).

### 3.4. Electrochemical impedance spectra (EIS)

One of the important roles of GO is acting as an electron acceptor and transfer channel to facilitate the separation and migration of photogenerated electrons [55–57], and thereby achieving a higher rate in the photodegradation of organic pollutants. We have measured the EIS spectra of the pure  $\text{Ag}_2\text{CrO}_4$  and  $\text{Ag}_2\text{CrO}_4$ -GO composites to investigate their charge transfer capability. As shown in Fig. 6, comparing with that of G0, the EIS Nyquist plots of G1 and G3 exhibit much smaller semicircles, indicating a significant decrease of the charge transfer resistance in the  $\text{Ag}_2\text{CrO}_4$ -GO composites. Notably, G1 shows the smallest semicircle, implying that there is an optimal GO content for the best charge transfer capability. The enlarged charge transfer resistance in G3 is due to the excessive addition of GO, which may act as new recombination centres of the photogenerated electrons and holes to hinder the migration of photogenerated electrons from the interior to the surface of the composite [58].

### 3.5. Photocatalytic activity and stability

It is well known that the adsorption property of a photocatalyst towards the pollutant molecules is one of the crucial factors to affect the photocatalytic activity. To investigate the adsorption properties of the obtained samples, their adsorption behaviours over MB in darkness were measured and presented in Fig. 7a. It can be found that the  $\text{Ag}_2\text{CrO}_4$ -GO composites exhibit gradually stronger adsorption properties with increasing the GO content. This is partially due to the non-covalent intermolecular  $\pi-\pi$  interactions between pollutant molecules and the GO sheets [9,59]. Moreover, the larger specific surface area and the more negative zeta potential of the composites compared with pure  $\text{Ag}_2\text{CrO}_4$  particles also facilitate the adsorption of the positively charged MB molecules.

The concentration changes of MB during the photodegradation process under visible-light irradiation are shown in Fig. 7b. A negligible photodegradation of MB is observed in the absence of any

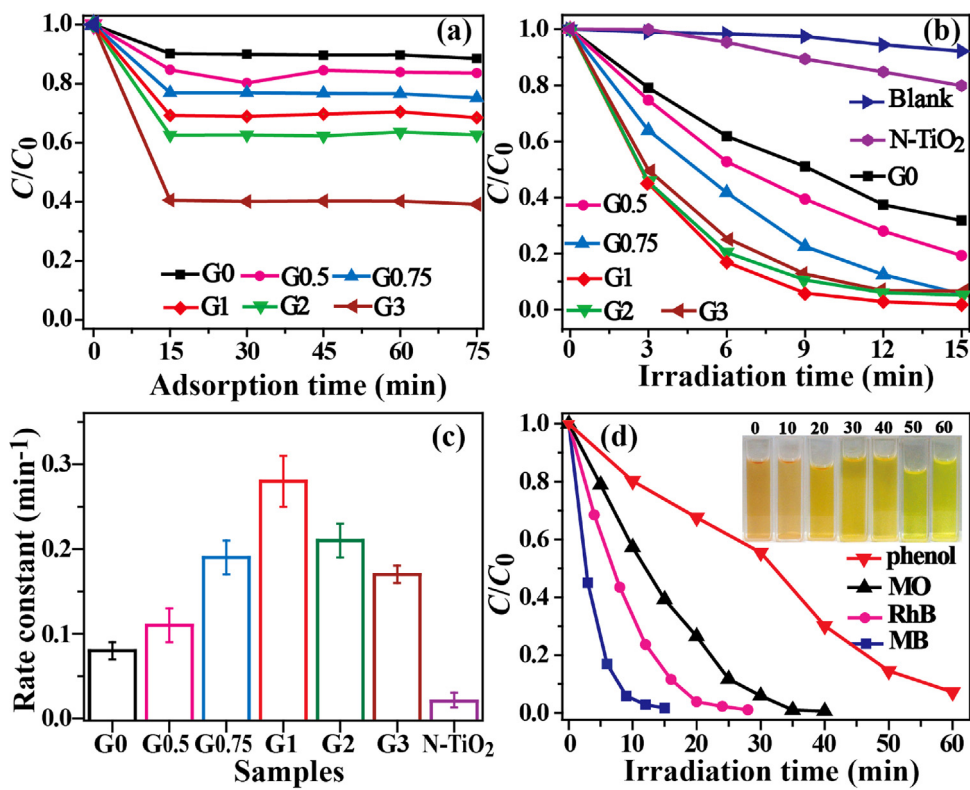


**Fig. 7.** (a) Adsorption properties of obtained samples under dark conditions. (b) The photocatalytic activities of obtained samples for MB degradation under visible-light irradiation. (c) The comparison of apparent rate constants ( $k$ ) of the obtained samples for MB degradation under visible-light irradiation. (d) A comparison of G1 on the photodegradation of phenol, MO, RhB and MB aqueous solution under visible-light irradiation (the insert is the corresponding colour changes of phenol aqueous solution with the irradiation time in the presence of the colour-developing agent). (For interpretation of the references to colour in this figure legend, the reader is referred to the web version of the article.)

photocatalyst. When N-TiO<sub>2</sub> and pure Ag<sub>2</sub>CrO<sub>4</sub> were employed as photocatalysts, about 20% and 70% of MB were decomposed after 15 min, respectively, suggesting that Ag<sub>2</sub>CrO<sub>4</sub> is a more efficient visible-light-driven photocatalyst because of its narrower band gap (~1.8 eV). After the introduction of GO, the Ag<sub>2</sub>CrO<sub>4</sub>-GO composites exhibit much higher photocatalytic activities, which can be explained by the following facts. Firstly, the capping effect of GO has reduced the particle size of Ag<sub>2</sub>CrO<sub>4</sub> and improved the dispersity of the composites. Secondly, GO has served as an ideal support to increase the specific surface area of the composites and provided abundant adsorption and catalytic sites for photocatalytic degradation. Thirdly, GO has also acted as a photo-absorber to extend the photo-absorption of the composites which may cause positive photo-thermal effect for the catalytic reaction. Finally, GO can serve as an efficient electron transfer channel and acceptor to suppress the recombination of the photogenerated carriers and facilitate the transfer of the photogenerated electrons. As a result, the synergistic effects between Ag<sub>2</sub>CrO<sub>4</sub> and GO significantly enhance the photocatalytic activity of the composites. Especially, the G1 sample shows the highest photocatalytic activity, with the complete degradation of MB within 15 min under visible-light irradiation.

The rate constants ( $k$ ) of all samples are calculated and presented in Fig. 7c, which firstly increase with increasing GO content until up to 1.0 wt% and then decrease at a higher GO content. Namely, the optimal composite with 1.0 wt% GO content possesses a rate constant of  $0.28 \text{ min}^{-1}$ , which is 3.5 and 14 times that of pure Ag<sub>2</sub>CrO<sub>4</sub> and N-TiO<sub>2</sub>, respectively. This result is in agreement with the EIS analysis. However, excessive loading of black-colour GO will shield the active sites on the catalyst surface and decrease the intensity of light through the depth of the reaction solution [17,52,60].

Therefore, it is crucial to control the ratios of GO in the composites to gain the best activity.

In order to investigate the universal application of the Ag<sub>2</sub>CrO<sub>4</sub>-GO photocatalyst, the G1 sample was further evaluated for the degradation of RhB, MO and phenol in aqueous solution, where RhB is another cationic dye in addition to MB, and MO is an anionic dye, while phenol is usually difficult to be degraded because of its stable benzene ring structure. For all experiments, the adsorption-desorption equilibrium was established before irradiation and the results showed that about 30%, 24%, 16% and 13% of MB, RhB, MO and phenol were adsorbed onto the surface of G1, respectively. Fig. 7d presents the comparison of G1 on the photodegradation of phenol, MO, RhB and MB aqueous solution under visible-light irradiation, where the data starts from the initial concentration of the pollutants after the adsorption-desorption equilibrium (i.e.  $C_0$ ). As shown in Fig. 7d, MB, RhB and MO could be completely degraded within 15, 28 and 40 min, respectively. It can be seen that G1 shows better photocatalytic degradation performance of MB and RhB than that of MO. This is because the negatively charged composite is much easier to adsorb the cationic dyes rather than anionic dyes. Furthermore, the photocatalytic degradation activity of MB is better than that of RhB, which is due to the more complicated and larger structures of the RhB molecules. More importantly, even 90% of phenol could also be photo-degraded by G1 within 60 min under visible-light irradiation. Here we assume two types of interactions between phenol and GO. (1)  $\pi-\pi$  stacking interaction between phenol molecules and GO sheets, and (2) hydrogen bonding between the phenolic hydroxyl and the oxygen functional groups of GO. These interactions could facilitate the adsorption of phenol onto the surface of GO, and Ag<sub>2</sub>CrO<sub>4</sub> and GO have close contact, thus promoting the degradation of phenol.

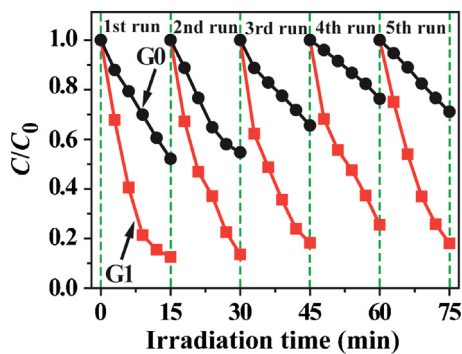


Fig. 8. Repeated photocatalytic experiments of G0 and G1.

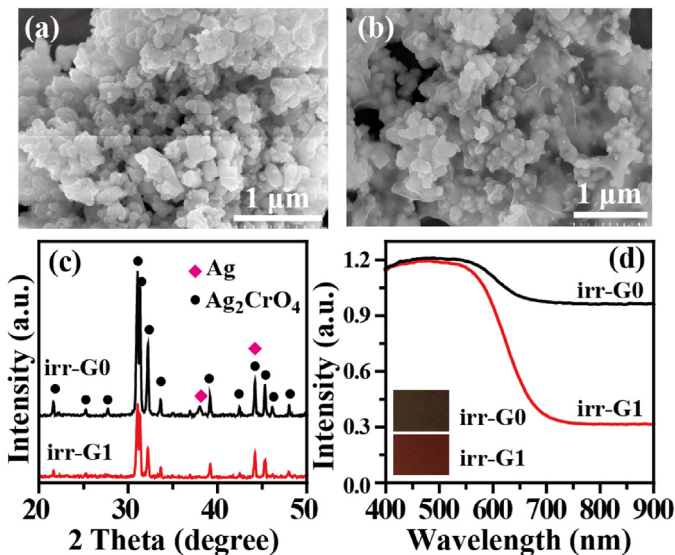


Fig. 9. SEM images of (a) irr-G0 and (b) irr-G1; (c) XRD patterns and (d) UV-visible diffuse reflectance spectra of irr-G0 and irr-G1 (the insert of (d) is their corresponding colours). (For interpretation of the references to colour in this figure legend, the reader is referred to the web version of the article.)

Considering the semiconductor property of GO, the blank experiments of GO (5 mg) serving as a photocatalyst to degrade MB, RhB, MO and phenol were also carried out. The results showed that about 18%, 16%, 13% and 26% of MB, RhB, MO and phenol were degraded in 15, 27, 40 and 60 min, respectively, suggesting a certain photocatalytic activity of GO for the degradation of the above dyes and phenol, however, which is far behind that of  $\text{Ag}_2\text{CrO}_4$ -GO composite. These results suggest the superiority of  $\text{Ag}_2\text{CrO}_4$ -GO photocatalyst on the degradation of persistent organic pollutants with high toxicity and low concentration.

The photocatalytic stability of the G0 and G1 samples was investigated by repeated photocatalytic experiments. As shown in Fig. 8, G1 exhibits not only much higher photocatalytic activity but also much higher stability than those of G0. Further analysis of SEM images, XRD patterns and DRS spectra for the G0 and G1 samples after repeated experiments (labelled as irr-G0 and irr-G1) are presented in Fig. 9. The SEM image of irr-G0 (Fig. 9a) shows a certain amount of aggregated particles with irregular morphology and sizes, suggesting the partial decomposition of  $\text{Ag}_2\text{CrO}_4$  during the photocatalytic reaction. Fortunately, the structure of irr-G1 remains relatively stable as shown in Fig. 9b. In the XRD patterns (Fig. 9c), a new diffraction peak located at  $2\theta = 38.1^\circ$  corresponding to the (111) plane of silver (JCPDS No. 65-2871) is observed for irr-G0, confirming that  $\text{Ag}_2\text{CrO}_4$  is partially decomposed to Ag. However, such peak does not appear for G1, indicating the good

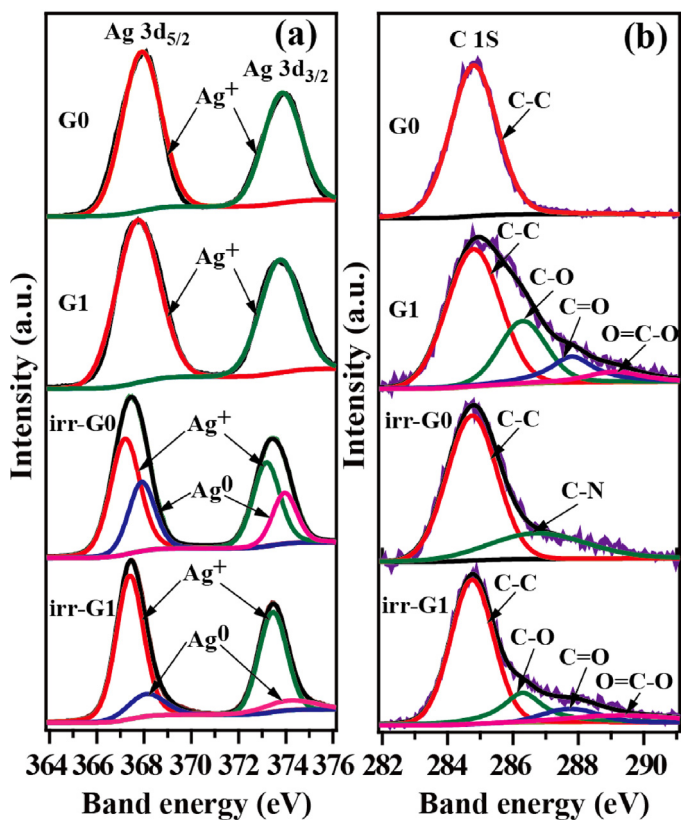


Fig. 10. XPS spectra of (a) Ag 3d and (b) C 1s of the samples obtained before (G0 and G1) and after (irr-G0 and irr-G1) repeated photocatalytic experiments.

photocatalytic stability of the  $\text{Ag}_2\text{CrO}_4$ -GO composite. In addition, Fig. 9d shows that the absorbance intensity of irr-G0 in the range of 600–900 nm largely increased because of the dark silver nanoparticles [8,26], which has been confirmed by the dark colour of irr-G0. In contrast, DRS spectrum and the corresponding colour of irr-G1 exhibit no obvious change as compared to those of G1 before photocatalytic experiments. These results demonstrate the excellent photocatalytic activity and stability of the  $\text{Ag}_2\text{CrO}_4$ -GO photocatalyst, in which the photocorrosion of  $\text{Ag}_2\text{CrO}_4$  is obviously inhibited by the introduction of GO.

To understand the mechanism of the enhanced photocatalytic stability of  $\text{Ag}_2\text{CrO}_4$  by GO introduction, the high-resolution XPS spectra of Ag 3d and C 1s of G0 and G1 before and after repeated photocatalytic experiments are measured. As shown in Fig. 10, The XPS spectra of Ag species of G0 and G1 display two peaks at ca. 367.9 and 373.9 eV corresponding to the binding energies of Ag 3d<sub>5/2</sub> and Ag 3d<sub>3/2</sub>, which belong to the  $\text{Ag}^+$ . For irr-G0 and irr-G1, two bands centred at 367.8 and 373.8 eV are observed, which can be further deconvoluted into two groups of peaks at 367.7, 368.4 eV and 373.7, 374.4 eV, respectively. The peaks at 367.7 (Ag 3d<sub>5/2</sub>) and 373.7 (Ag 3d<sub>3/2</sub>) eV are ascribed to  $\text{Ag}^+$ , and those peaks at 368.4 (Ag 3d<sub>5/2</sub>) and 374.4 (Ag 3d<sub>3/2</sub>) eV are related to the  $\text{Ag}^0$  [22,24,25]. The thus-calculated surface molar ratio of  $\text{Ag}^0$  to  $\text{Ag}^+$  is ca. 56% for irr-G0, whereas decreases remarkably to ca. 15% for irr-G1, confirming that the photocorrosion of  $\text{Ag}_2\text{CrO}_4$  is effectively inhibited via GO introduction, which results in much less generation of  $\text{Ag}^0$  after photocatalytic reaction. On the other hand, the C 1s XPS spectrum of G0 indicates only a non-oxygenated C-C bond locating at 284.8 eV, which results from the C pollution. After repeated photocatalytic experiments, a new peak at 287.1 eV corresponding to the C-N bond can be observed for irr-G0 [61], which might originate from the residual MB. For G1 and irr-G1, three characteristic peaks located at 286.3, 287.8 and 289.1 eV are observed,

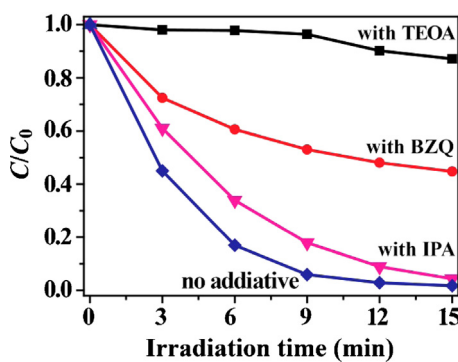


Fig. 11. Reactive species trapping experiments of G1.

corresponding to the C–O, C=O and O=C–O functional groups of typical GO sheets, respectively. However, the intensities of these characteristic peaks of irr-G1 distinctly decrease as compared to those of G1, suggesting that GO is partially reduced and changes to reduced graphene oxide (rGO) after repeated photocatalytic experiments. These observations demonstrate that GO indeed acts as an electron acceptor and transfer channel to promote the photo-generated electron–hole separation, resulting in the enhancement on the photocatalytic activity and stability of  $\text{Ag}_2\text{CrO}_4$ .

### 3.6. Photocatalytic mechanism

Reactive species trapping experiments were performed to investigate the reactive oxygen species during the photocatalytic process. Particularly, triethanolamine (TEOA, 0.01 M), *p*-benzoquinone (BZQ, 0.001 M) and isopropanol (IPA, 0.02 M) were employed as scavengers for photogenerated holes ( $\text{h}^+$ ), superoxide anion radicals ( $\bullet\text{O}_2^-$ ) and hydroxyl radicals ( $\bullet\text{OH}$ ), respectively. The experimental results (Fig. 11) show that the addition of TEOA into the photocatalytic system caused fast deactivation of the  $\text{Ag}_2\text{CrO}_4$ -GO composite, indicating photogenerated holes are the predominant active species. Moreover, the introduction of BZQ into the photocatalytic system could also decrease the photocatalytic degradation of MB from almost 100% to 50% in 15 min, suggesting  $\bullet\text{O}_2^-$  also plays an important role in the photocatalytic process. However, only a weak inhibition was observed on the photodegradation of MB when IPA was introduced into the photocatalytic system, implying that  $\bullet\text{OH}$  makes very small contribution to the photocatalytic reaction.

On the basis of the Mott-Schottky equation, the flat-band positions of the samples can be determined from the linear potential plots [62], as shown in Fig. 12. The positive slope of the straight lines indicates that  $\text{Ag}_2\text{CrO}_4$  is an n-type semiconductor, whose lowest potential of the CB can be approximately estimated to equate with the flat-band potential [63]. Thus, the CB level of  $\text{Ag}_2\text{CrO}_4$  is measured to be ca. 0.47 V (vs NHE) and the VB level is calculated to be ca. 2.27 V (vs NHE). It has been demonstrated that GO is a semiconductor with a band gap of ca. 2.5 eV, whose CB and VB levels are ca. –0.75 and 1.75 V (vs NHE) [31,32], respectively. Because the CB level of  $\text{Ag}_2\text{CrO}_4$  is less negative than the  $\bullet\text{O}_2^-/\text{O}_2$  potential (–0.28 V) [64], it is difficult for  $\text{Ag}_2\text{CrO}_4$  to reduce the adsorbed  $\text{O}_2$  to produce  $\bullet\text{O}_2^-$ . Fig. 12 shows that after the introduction of GO, the CB levels of the composites change only a little bit, still with insufficient reduction ability for  $\bullet\text{O}_2^-$  production. However, the reactive species trapping experiments have demonstrated that  $\bullet\text{O}_2^-$  radicals play an important role in the photocatalytic process. These observations imply a different transfer route of photogenerated electrons existing in the  $\text{Ag}_2\text{CrO}_4$ -GO composite photocatalyst.

Herein, a Z-scheme mechanism for the enhanced photocatalytic activity and stability of  $\text{Ag}_2\text{CrO}_4$ -GO composites is proposed, as

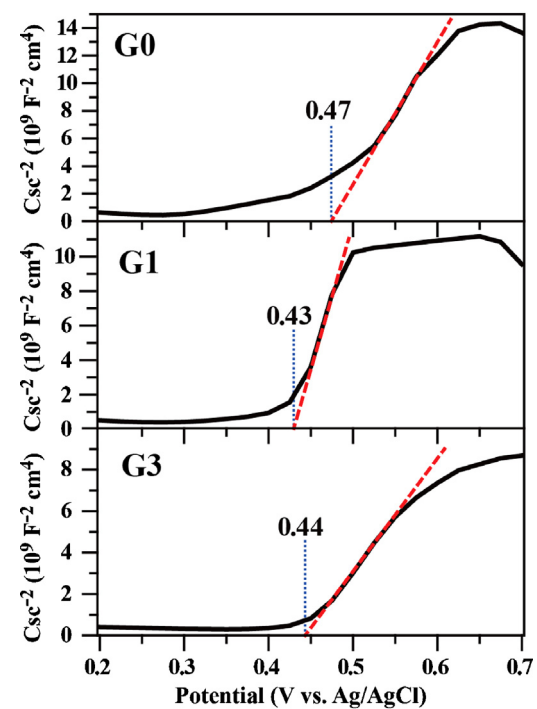


Fig. 12. The Mott-Schottky plots of G0, G1 and G3 for determining the flat-band potentials of samples.

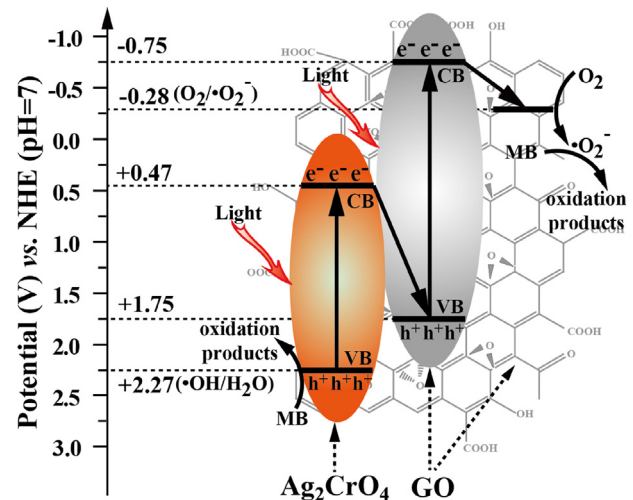


Fig. 13. Z-scheme photocatalytic mechanism for  $\text{Ag}_2\text{CrO}_4$ -GO composite photocatalysts.

illustrated in Fig. 13. Due to their narrow band gaps, both  $\text{Ag}_2\text{CrO}_4$  and GO can be easily excited to yield photogenerated electron–hole pairs under visible-light irradiation. Since both the CB and VB positions of  $\text{Ag}_2\text{CrO}_4$  are lower than those of GO, the photogenerated electrons ( $e^-$ ) in the CB of  $\text{Ag}_2\text{CrO}_4$  tend to transfer and recombine with the photogenerated holes ( $\text{h}^+$ ) in the VB of GO. As such, the photogenerated holes left behind in the VB of  $\text{Ag}_2\text{CrO}_4$  can directly oxidize MB to harmless products. Simultaneously, the remained photogenerated electrons in the CB of GO can reduce the adsorbed  $\text{O}_2$  to yield  $\bullet\text{O}_2^-$ , which is a powerful oxidative species for MB degradation. However, compared to the  $\bullet\text{OH}/\text{H}_2\text{O}$  potential (ca. 2.27 V) [64], the VB levels of  $\text{Ag}_2\text{CrO}_4$  and GO are both not positive enough to drive the oxidation process of  $\text{H}_2\text{O}$  to form  $\bullet\text{OH}$  due to their insufficient oxidation ability, which is also confirmed by the photoluminescence technique using coumarin as a probe molecule to

detect •OH [65]. The results showed that no noticeable •OH could be detected in the photocatalytic reaction here. This explains why •OH has a negligible effect on the photocatalytic performance. It can be concluded that the photocatalytic reaction in the presence of Ag<sub>2</sub>CrO<sub>4</sub>-GO composites followed a typical Z-scheme mechanism, which enables a fast separation and transfer of the photogenerated electron-hole pairs and meanwhile a strong oxidation and reduction ability for efficient photocatalytic degradation of organic pollutants [66]. Furthermore, the fast transfer of photogenerated electrons from Ag<sub>2</sub>CrO<sub>4</sub> to the GO sheets before Ag<sup>+</sup> is reduced to Ag<sup>0</sup> successfully inhibits the photocorrosion of Ag<sub>2</sub>CrO<sub>4</sub> and thus gives rise to an improved stability of the composites.

#### 4. Conclusions

In summary, Ag<sub>2</sub>CrO<sub>4</sub>-GO composites are successfully synthesized using a facile precipitation method and exhibit excellent photocatalytic activity and stability for the decomposition of organic pollutants. The composite with the optimal 1.0 wt% GO content exhibits the highest photocatalytic activity towards MB degradation, which can be achieved within 15 min. The introduction of GO has resulted in the formation of Z-scheme Ag<sub>2</sub>CrO<sub>4</sub>-GO heterojunctions that possess higher efficiency of charge separation and transfer, as well as stronger oxidation and reduction ability. Moreover, the photocorrosion of Ag<sub>2</sub>CrO<sub>4</sub> particles is obviously inhibited by transferring the photogenerated electrons of Ag<sub>2</sub>CrO<sub>4</sub> to GO. As a result, both the photocatalytic activity and stability have been greatly improved for the Ag<sub>2</sub>CrO<sub>4</sub>-GO composites as compared to those of pure Ag<sub>2</sub>CrO<sub>4</sub> particles. This work may give a new insight into the development of GO/silver compound composite photocatalysts for various applications.

#### Acknowledgments

This work was supported by the 973 Program (2013CB632402), and NSFC (51320105001, 51372190, 51402025 and 21177100). Also, this work was financially supported by the General Financial Grant from the China Postdoctoral Science Foundation (2014M552101), the Fundamental Research Funds for the Central Universities (WUT: 2014-VII-010, 2014-IV-058), Self-determined and Innovative Research Funds of SKLWUT (2013-ZD-1), and a WUT Start-Up Grant.

#### References

- [1] M.R. Hoffmann, S.T. Martin, W. Choi, D.W. Bahnemann, *Chem. Rev.* 95 (1995) 69.
- [2] Z.G. Yi, J.H. Ye, N. Kikugawa, T. Kako, S.X. Ouyang, H. Stuart-Williams, H. Yang, J.Y. Cao, W.J. Luo, Z.S. Li, Y. Liu, R.L. Withers, *Nat. Mater.* 9 (2010) 559.
- [3] M.C. Long, W.M. Cai, *Nanoscale* 6 (2014) 7730.
- [4] S.X. Ouyang, Z.S. Li, Z. Ouyang, T. Yu, J.H. Ye, Z.G. Zou, *J. Phys. Chem. C* 112 (2008) 3134.
- [5] Y. Liu, H.B. Yu, M. Cai, J.W. Sun, *Catal. Commun.* 26 (2012) 63.
- [6] F. Soofivand, F. Mohandes, M. Salavati-Niasari, *Mater. Res. Bull.* 48 (2013) 2084.
- [7] D.F. Xu, S.W. Cao, J.F. Zhang, B. Cheng, J.G. Yu, *Beilstein J. Nanotechnol.* 5 (2014) 658.
- [8] G.P. Dai, J.G. Yu, G. Liu, *J. Phys. Chem. C* 116 (2012) 15519.
- [9] Q.J. Xiang, J.G. Yu, M. Jaroniec, *Chem. Soc. Rev.* 41 (2012) 782.
- [10] J.X. Low, S.W. Cao, J.G. Yu, S. Wageh, *Chem. Commun.* 50 (2014) 10768.
- [11] W.G. Wang, J.G. Yu, Q.J. Xiang, B. Cheng, *Appl. Catal. B* 119–120 (2012) 109.
- [12] T.N. Lambert, C.A. Chavez, B. Hernandez-Sanchez, P. Lu, N.S. Bell, A. Ambrosini, T. Friedman, T.J. Boyle, *J. Phys. Chem. C* 113 (2009) 19812.
- [13] C. Chen, W.M. Cai, M.C. Long, B.X. Zhou, Y.H. Wu, D.Y. Wu, Y.J. Feng, *ACS Nano* 4 (2010) 6425.
- [14] G.D. Jiang, Z.F. Lin, C. Chen, L.H. Zhu, Q. Chang, N. Wang, W. Wei, H.Q. Tang, *Carbon* 49 (2011) 2693.
- [15] G. Williams, P.V. Kamat, *Langmuir* 25 (2009) 13869.
- [16] Q. Li, B.D. Guo, J.G. Yu, J.R. Ran, B.H. Zhang, H.J. Yan, J.R. Gong, *J. Am. Chem. Soc.* 133 (2011) 10878.
- [17] T.Y. Peng, K. Li, P. Zeng, Q.G. Zhang, X.G. Zhang, *J. Phys. Chem. C* 116 (2012) 22720.
- [18] R.A. He, S.W. Cao, P. Zhou, J.G. Yu, *Chin. J. Catal.* 35 (2014) 989.
- [19] J.Y. Liu, Y. Bai, P.Y. Luo, P.Q. Wang, *Catal. Commun.* 42 (2013) 58.
- [20] S. Chen, J.J. Duan, W. Han, S.Z. Qiao, *Chem. Commun.* 50 (2014) 207.
- [21] S. Chen, J.W. Zhu, X.D. Wu, Q.F. Han, X. Wang, *ACS Nano* 4 (2010) 2822.
- [22] M.S. Zhu, P.L. Chen, M.H. Liu, *ACS Nano* 5 (2011) 4529.
- [23] C.Y. Zeng, M. Guo, B.Z. Tian, J.L. Zhang, *Chem. Phys. Lett.* 575 (2013) 81.
- [24] M.S. Zhu, P.L. Chen, M.H. Liu, *Langmuir* 28 (2012) 3385.
- [25] M.S. Zhu, P.L. Chen, M.H. Liu, *Langmuir* 29 (2013) 9259.
- [26] X.F. Yang, H.Y. Cui, Y. Li, J.L. Qin, R.X. Zhang, H. Tang, *ACS Catal.* 3 (2013) 363.
- [27] Y. Hou, F. Zou, Q. Ma, C. Wang, L. Bartels, P.Y. Feng, *J. Phys. Chem. C* 116 (2012) 20132.
- [28] P.Y. Dong, Y.H. Wang, B.C. Cao, S.G. Xin, L.N. Guo, J. Zhang, F.H. Li, *Appl. Catal. B* 132–133 (2013) 45.
- [29] C. Dong, K.L. Wu, X.W. Wei, X.Z. Li, L. Liu, T.H. Ding, J. Wang, Y. Ye, *CrystEngComm* 16 (2014) 730.
- [30] Y.X. Song, J.X. Zhu, H. Xu, C. Wang, Y.G. Xu, H.Y. Ji, K. Wang, Q. Zhang, H.M. Li, *J. Alloys Compd.* 592 (2014) 258.
- [31] T.F. Yeh, J.M. Syu, C. Cheng, T.H. Chang, H. Teng, *Adv. Funct. Mater.* 20 (2010) 2255.
- [32] T.F. Yeh, F.F. Chan, C.T. Hsieh, H. Teng, *J. Phys. Chem. C* 115 (2011) 22587.
- [33] P. Zhou, J.G. Yu, M. Jaroniec, *Adv. Mater.* 26 (2014) 4920.
- [34] Y.L. Min, G.Q. He, Q.J. Xu, Y.C. Chen, *J. Mater. Chem. A* 2 (2014) 1294.
- [35] W.S. Hummers, R.E. Offeman, *J. Am. Chem. Soc.* 80 (1958) 1339.
- [36] X.F. Wang, S.F. Li, H.G. Yu, J.G. Yu, *J. Mol. Catal. A* 334 (2011) 52.
- [37] X.T. Hong, Z.P. Wang, W.M. Cai, F. Lu, J. Zhang, Y.Z. Yang, N. Ma, Y.J. Liu, *Chem. Mater.* 17 (2005) 1548.
- [38] M. Ge, N. Zhu, Y.P. Zhao, J. Li, L. Liu, *Ind. Eng. Chem. Res.* 51 (2012) 5167.
- [39] T.A. Pham, B.C. Choi, Y.T. Jeong, *Nanotechnology* 21 (2010) 465603.
- [40] A.C. Ferrari, J. Robertson, *Phys. Rev. B* 61 (2000) 14095.
- [41] R.L. Carter, *Spectrosc. Lett.* 5 (1972) 401.
- [42] D. Santamaría-Pérez, E. Bandiello, D. Errandonea, J. Ruiz-Fuertes, O. Gomis, J.A. Sans, F.J. Manjón, P. Rodríguez-Hernández, A. Muñoz, *J. Phys. Chem. C* 117 (2013) 12239.
- [43] Y.W. Zhu, S. Murali, W.W. Cai, X.S. Li, J.W. Suk, J.R. Potts, R.S. Ruoff, *Adv. Mater.* 22 (2010) 3906.
- [44] X.J. Lv, W.F. Fu, H.X. Chang, H. Zhang, J.S. Cheng, G.J. Zhang, Y. Song, C.Y. Hu, J.H. Li, *J. Mater. Chem.* 22 (2012) 1539.
- [45] H. Zhang, X.F. Fan, X. Quan, S. Chen, H.T. Yu, *Environ. Sci. Technol.* 45 (2011) 5731.
- [46] L.J. Cote, J. Kim, V.C. Tung, J.Y. Luo, F. Kim, J.X. Huang, *Pure Appl. Chem.* 83 (2011) 95.
- [47] E.C. Vermisoglou, E. Devlin, T. Giannakopoulou, G. Romans, N. Boukos, V. Psycharis, C. Lei, C. Lekakou, D. Petridis, C. Trapalis, *J. Alloys Compd.* 590 (2014) 102.
- [48] K.S.W. Sing, D.H. Everett, R. Haul, L. Moscou, R.A. Pierotti, J. Rouquerol, T. Siemiewska, *Pure Appl. Chem.* 57 (1985) 603.
- [49] Q. Li, H. Meng, J.G. Yu, W. Xiao, Y.Q. Zheng, J. Wang, *Chem. Eur. J.* 20 (2014) 1176.
- [50] Y. Wang, R. Shi, J. Lin, Y.F. Zhu, *Appl. Catal. B* 100 (2010) 179.
- [51] H.T. Yu, S. Chen, X.F. Fan, X. Quan, H.M. Zhao, X.Y. Li, Y.B. Zhang, *Angew. Chem. Int. Ed.* 49 (2010) 5106.
- [52] T.G. Xu, L.W. Zhang, H.Y. Cheng, Y.F. Zhu, *Appl. Catal. B* 101 (2011) 382.
- [53] Y. Ou, J.D. Lin, S.M. Fang, D.W. Liao, *Chem. Phys. Lett.* 429 (2006) 199.
- [54] K. Dai, T.Y. Peng, D.N. Ke, B.Q. Wei, *Nanotechnology* 20 (2009) 125603.
- [55] J.G. Yu, J. Jin, B. Cheng, M. Jaroniec, *J. Mater. Chem. A* 2 (2014) 3407.
- [56] Q.J. Xiang, J.G. Yu, M. Jaroniec, *J. Am. Chem. Soc.* 134 (2012) 6575.
- [57] W.J. Wang, J.C. Yu, D.H. Xia, P.K. Wong, Y.C. Li, *Environ. Sci. Technol.* 47 (2013) 8724.
- [58] X.Y. Zhang, H.P. Li, X.L. Cui, Y.H. Lin, *J. Mater. Chem.* 20 (2010) 2801.
- [59] H. Zhang, X.J. Lv, Y.M. Li, Y. Wang, J.H. Li, *ACS Nano* 4 (2010) 380.
- [60] Q.J. Xiang, J.G. Yu, *J. Phys. Chem. Lett.* 4 (2013) 753.
- [61] E. Riedo, F. Comin, J. Chevrier, F. Schmidthusen, S. Decossas, M. Sancrotti, *Surf. Coat. Technol.* 125 (2000) 124.
- [62] K. Gelderman, L. Lee, S.W. Donne, *J. Chem. Edu.* 84 (2007) 685.
- [63] S. Sakthivel, H. Kisch, *Angew. Chem. Int. Ed.* 42 (2003) 4908.
- [64] A. Fujishima, X.T. Zhang, C.R. Chiu, *Mater. Sci. Eng. B* 9 (2006) 750.
- [65] Q.J. Xiang, J.G. Yu, P.K. Wong, *J. Colloid Interface Sci.* 357 (2011) 163.
- [66] F.Y. Xu, W. Xiao, B. Cheng, J.G. Yu, *Int. J. Hydrogen Energy* 39 (2014) 15394.